Forming a Mogi Doughnut in the years prior to and immediately before the the 2014 M8.1 Iquique, Northern Chile Earthquake

B. Schurr[1], M. Moreno[2], A. M. Tréhu[3], J. Bedford[1], J. Kummerow[4], S. Li[5], and O. Oncken[1]

[1]Deutsches GeoForschungsZentrum – GFZ, Section Lithosphere Dynamics, Telegrafenberg, 14473 Potsdam, Germany

[2]Universidad de Concepción, Departamento de Geofísica, Concepción, Chile

[3]Oregon State University, College of Earth, Ocean, and Atmospheric Sciences, Corvallis, USA

[4]Freie Universität Berlin, Department of Earth Sciences, Berlin, Germany

[5]The University of Tokyo, Earthquake Research Institute, Tokyo, Japan

Corresponding author: Bernd Schurr (schurr@gfz-potsdam.de)

Key Points:

- Seismicity in the years prior to and immediately before the mainshock form two halves of a "Mogi Doughnut" surrounding the main slip patch
- Mechanical asperity model predicts stress increase under slab pull forces where earthquakes are observed
- Slip region correlates with high inter-seismic locking and a circular gravity low, suggesting that the asperity is controlled by geologic structure

Abstract

Asperities are patches where the fault surfaces stick until they break in earthquakes. Locating asperities and understanding their causes in subduction zones is challenging because they are generally located offshore. We use seismicity, inter- and co-seismic slip, and the residual gravity field to map the asperity responsible for the 2014 M8.1 Iquique Chile earthquake. Until two weeks before the mainshock, seismicity occurred exclusively down-dip of the asperity, until a foreshock series broke first the upper plate and later its updip rim. Together the seismicity formed a ring around the future earthquake's main slip patch. The asperity correlates both with high inter-seismic locking and a circular gravity low, suggesting that it is controlled by geologic structure. Most features of the spatiotemporal seismicity pattern can be explained by a mechanical model in which a single strong asperity is stressed by slab pull.

1 Introduction

Earthquakes are thought to be frictional instabilities on a fault surface. Asperities are patches on this surface defined as frictionally "strong," which stick until suddenly failing when the yield stress is reached (Lay & Kanamori, 1981). The configuration of these asperities is thought to be a main factor determining the distribution, size, and recurrence interval of large earthquakes (Thatcher, 1990). Asperities are generally recognized either by modeling inter-seismic surface deformation to infer inter-plate locking or, in hindsight, as being co-located with regions of large co-seismic slip. In subduction zones, large asperities are mostly located offshore (e.g., Schurr et al., 2012) and near-fault measurements are almost always onshore; therefore, their location, shape, size and amplitude are notoriously under-constrained. Despite the significance of asperities, fundamental aspects about their nature are poorly understood: It is not known whether they are persistent, caused, for example, by large-scale fault surface topography or frictional heterogeneities due to lithology or rheology in the fault zone, or whether they are ephemeral features controlled by processes such as pore pressure or stress heterogeneities. Although observational capabilities near faults have improved, there is little high resolution, long-term data that monitors the evolution of an asperity as it prepares to rupture. Stressing an asperity changes the spatiotemporal distribution of background seismicity (Dmowska & Lovison, 1992; Kanamori, 2013). A detailed analysis of seismicity patterns, therefore, may provide clues about the stress patterns in the fault zone.

The rupture region of the Mw 8.1 Iquique earthquake had been monitored for more than seven years before the mainshock by the Integrated Plate boundary Observatory Chile (IPOC) (GFZ and CNRS-INSU, 2006), providing a unique opportunity to study the spatio-temporal relationships between background seismicity, geodetically-derived locking, foreshock activity, and mainshock rupture. Due to the wealth of these observational data, the Iquique earthquake sequence has been extensively studied (e.g., Duputel et al., 2015; Hayes et al., 2014; Herman et al., 2015; Jara et al., 2018; Lay et al., 2014; Meng et al., 2015; Ruiz et al., 2014; Schurr et al., 2014; Soto et al., 2019; Yagi et al., 2014). It broke a central portion of the approximately 500 km long segment that ruptured last in the great 1877 northern Chile megathrust event (Ruiz & Madariaga, 2018). Published models for the cumulative slip of the mainshock generally agree on a single main slip patch south of the epicenter, which differs in size and amplitude depending on the choice of and weighting among the different available data sets (see Duputel et al., 2015 and Figure S1 for examples). Duputel et al. (2015) utilized the most comprehensive co-seismic observations combining seismic, geodetic and tsunami data. They applied a Bayesian inversion

scheme thereby omitting regularization, which tends to smooth and broaden slip models. Their model suggests that as much as 12 m of slip was concentrated in a relatively small area, resulting in a high stress drop (>10 MPa). The slip region seems to correlate with a region of high inter-seismic locking (Li et al., 2015; Ruiz et al., 2014; Schurr et al., 2014; this study, Figure 1f). The Iquique mainshock was heralded by two weeks of intense foreshock activity, which we refer to as the pre-seismic period, in contrast to the decadal inter-seismic period (Figure 1g). The late inter- and pre-seismic activity was accompanied by transient surface deformation observed on continuous GPS receivers close to the Chilean coast (Bedford et al., 2015; S. Ruiz et al., 2014; Socquet et al., 2017).

Here we study for the first time the long-term background seismicity in the region of the Iquique earthquake and show that it provides an important missing piece relating the foreshock sequence to the mainshock rupture. We combine these observations with an updated model of inter-seismic locking, detections of repeating earthquakes in the inter- and pre-seismic periods, residual gravity data, and a mechanical model that explains the spatio-temporal distribution of seismicity, including the location of the first large foreshock. Our combination of observations and models may provide the most detailed information to date on the process of stressing and rupturing a subduction zone asperity.

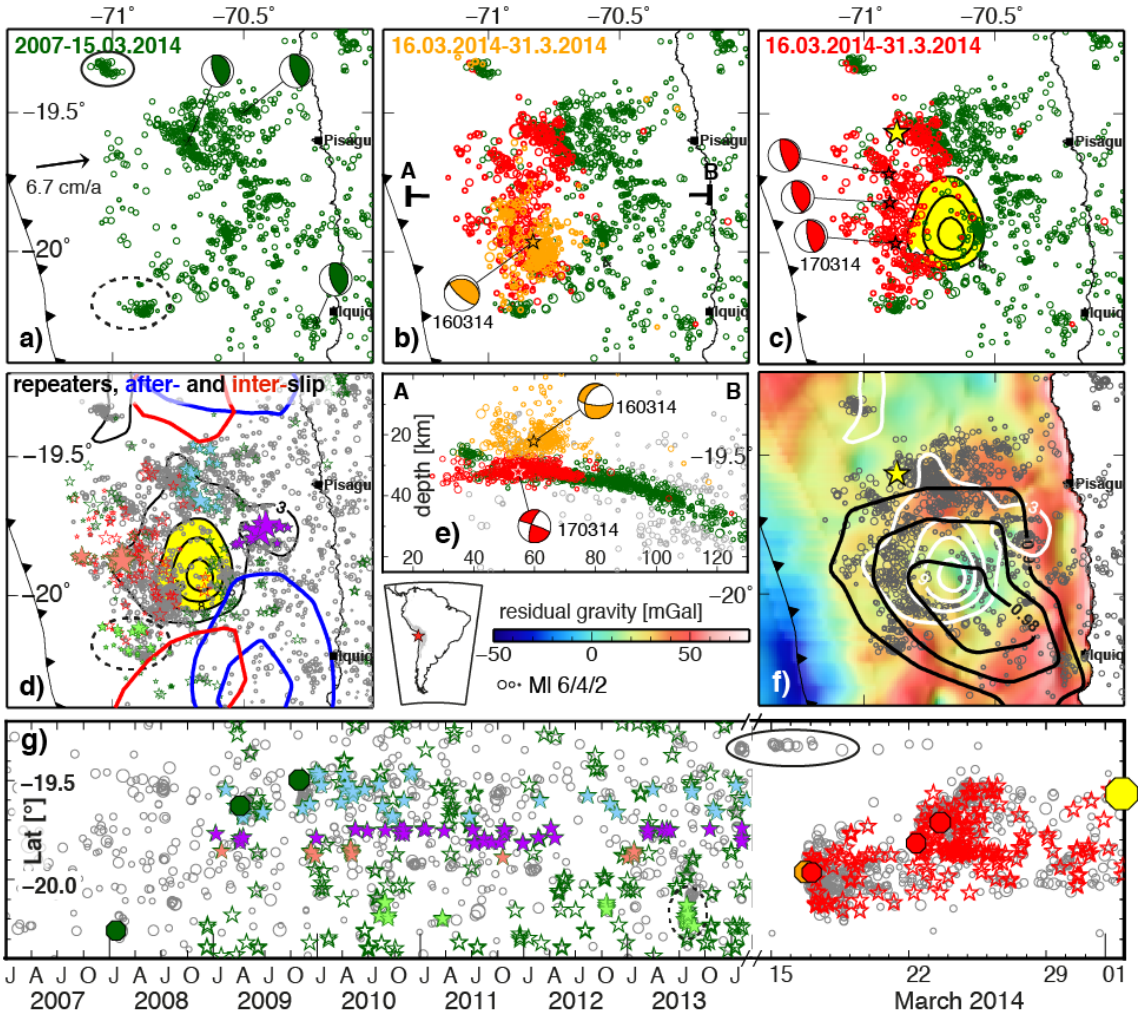

Figure 1. **a)** Inter-seismic seismicity in the Iquique earthquake rupture region on the plate interface (see Fig. 1e) from 2007 to 15/03/2014, i.e. one day before the M6.7 foreshock and two weeks before the mainshock. Two clusters discussed in text are marked. Source mechanisms of earthquakes with Mw>6 are shown as beachballs. **b)** Same as a) but with the pre-seismic foreshocks added. Presumed upper plate events are orange, inter-plate events are red (see Fig. 1e). Beachball and orange star mark the first M6.7 foreshock. Location of cross section in 1e) is indicated. **c)** Same as b) but presumed upper plate events are removed. Beachballs for foreshocks with M>6. Contours mark 6, 9, and 12 meters of mainshock slip (Duputel et al., 2015). Yellow star marks mainshock epicenter. **d)** Stars mark repeater sequences in the inter- (green) and pre-seismic (red) periods. Symbol size is scaled by number of repeaters per sequence (2-7). Symbol filling allows to identify clusters in Fig. 1g). Red contours outline 5 mm inter-seismic slip (Socquet et al., 2017), blue contours outline 60/80 cm post-seismic slip (Hoffmann et al., 2018). **e)** Cross section through inter- and pre- seismic activity. The two first large foreshocks of M6.7 and M6.3 are marked with stars and beachballs. **f)** Residual gravity anomalies, mainshock slip (white contours), inter-seismic plate locking degree (black) and pre-event seismicity (grey). **g)**

Time vs. latitude for pre-event seismicity (circles) and repeaters (stars). Colors as in Fig. 1d). Note, scaling of time axis changes on 15/03/2014. Same clusters as in a) are marked.

2 Data, Analysis and Results

2.1 Seismicity

We used the IPOC seismic network and additional permanent and temporary stations in the region to analyze background seismicity in the Iquique source region from January 1st 2007 until the April 1st 2014 mainshock. To detect, locate and relocate events with sequentially improved phase picks and locations, we used a multi-stage automatic procedure (Sippl et al., 2013). The catalog differs from the one published by (Sippl et al., 2018) in having less stringent event definition criteria at the detection stage and therefore contains more events (3050 events for the map extent displayed in Figure 1). We used a 1D velocity model developed for the northern Chilean forearc by Husen et al. (1999). In the final stage, the catalogue was relocated using the double-difference algorithm with cross correlation based differential travel times (Waldhauser & Ellsworth, 2000).

Seismicity from January 1st 2007 until March 15th, 2014 (just before the first large foreshock) is shown in Figure 1a. The region offshore the coastal towns of Pisagua and Iquique was seismically active during the entire observation period, featuring three plate-interface thrust events with M_w>6 in 2008 and 2009, one of which was close to the 2014 mainshock epicenter. Most hypocenters follow a well-defined surface (Figure S2) down-dip of the impending 2014 rupture zone, which we define based on Duputel et al.'s (2015) slip model (Figure 1). In addition, clusters of activity at the northern and southern flanks of the 2014 rupture zone were observed in July and August 2013 and in February and March 2014 (see circled clusters in Figures 1a and 1g).

On March 16th 2014 a Mw 6.7 earthquake initiated the foreshock sequence plotted in red and orange in Figure 1. The epicenter of the first foreshock was located just up-dip of what would be the zone of highest slip during the mainshock. Within a few hours, another Mw 6.3 event broke at ~5 km epicentral distance to the north. Although depth resolution of offshore events is hampered by the lack of offshore stations close to the epicenters, background seismicity preceding the foreshocks defines a landward-dipping plane in cross-section, which we interpret as the megathrust (Figures 1e, S2). The apparent flattening of this plane towards the trench is an artifact of the 1D velocity model. The March 2014 foreshock clearly locates above this plane whereas the next largest event (17 March 2014) falls on the plane. The mechanism for the latter event is compatible with inter-plate motion on the megathrust (Figure 1c, e). We corroborate the significant difference in depth and mechanism for these two events by long-period waveform modeling (Nábělek & Xia, 1995), which is less sensitive to the station distribution and velocity model (Figure S3). Over the following days, a cloud of events formed above the plate interface near the March 16th 2014 foreshock hypocenter (orange in Figure 1b,e), while seismicity on the presumed plate interface (red in Figure 1b,c,e) spread north and includes two more events of Mw > 6 with low angle thrust mechanisms (Figure 1c). The final foreshock stage included a NW-striking linear cluster of events that represents reactivation of an earlier cluster. The mainshock rupture initiated at the edge of this cluster (Figure 1c).

The inter-seismic events and foreshock sequence form a ring of seismicity that encircles a quiet zone (Figure 1b,c). This zone is almost perfectly filled by the high slip (>6 m) patch of the

mainshock (Figure 1b). This is even more obvious when only events interpreted to be on the megathrust surface are included (Figure 1c). Although we choose here the slip model based on the most complete data set (Duputel et al., 2015), the correlation also holds for other models (Figure S1). Such pre-seismic patterns, in which a ring of high seismicity surrounds a quiet patch, are well known (Kanamori, 2013; Mogi, 1969) and often termed 'Mogi doughnuts'.

2.2 Repeating earthquakes

We searched for repeating earthquakes as indicators of creeping sections or episodes on the plate interface. We use waveforms from the favorably located station PB11, which started operating in late 2008. As event templates, all events from the catalog of Sippl et al. (2018), which also contains nine months of the aftershock sequence, were used. This inventory covers the subduction fault comprehensively, allowing searching for similar, possibly weak events in regions that were mostly quiet during the inter-seismic period. For the templates, we cut a 35 s time window starting 5 s before the *P* arrival and including the *S* wave and applied a bandpass filter between 1 and 4 Hz. For each filtered template waveform, we ran a cross-correlation detector and classified an event as similar if the normalized cross-correlation coefficient exceeded a value of 0.95.

We identified 432 repeater sequences with up to seven events that were activated before the mainshock (Figure 1d, g). We subdivide and color-outline the repeater sequences in the same way as the earthquakes in inter-seismic and pre-seismic periods in Figure 1 and use color fillings to identify clusters in the map (Figure 1d) and latitude-time view (Figure 1g). At the northern margin of the asperity, near the epicenter, repeater clusters in light blue occurred primarily within a year following two M6 events in 2009 and again in summer 2013 and early 2014 (Figure 1d,g). Updip (west) of the asperity, where few earthquakes occurred during the inter-seismic period, the templates detect a number of repeater clusters mostly active in bursts in early and middle 2010 (when the northern clusters were also active) and early 2013, indicating discontinuous stressing. The region directly down-dip (east) of the asperity contains a number of repeating events, in particular in a streak-like cluster encircled by the 3 m slip contour (purple filled stars in Figure 1d). These repeaters were almost continuously active during the observation period (Figure 1g). Assuming that repeaters are loaded by creep, this indicates rather continuous slip at the downdip edge of the asperity. Two repeater clusters south of the asperity (light green) were active at three times with the largest with the highest activity accompanying two earthquake streaks that became active in summer 2013 and later during the foreshock sequence. These event streaks were also active post-seismically (Soto et al. 2019).

2.2 Modeling the inter-seismic locking state

Highs in inter-seismic locking maps derived by modeling GPS-measured surface displacements provide the most direct indication of megathrust asperities. We updated the inter-seismic visco-elastic locking model of Li et al. (2015) using a combination of new GPS-derived velocities from ~40 continuously recording sites, ~70 survey-type sites, and previously published vectors (Figure S4) (Kendrick et al., 2001; Métois et al., 2013). We used a 3D-spherical Finite Element Model (FEM) and created viscoelastic Green's Functions (following Li et al., 2015) with the solver Pylith (Aagaard et al., 2013). The geometry and configuration of our 3D model (Figure S5b, c) is based on the model of Li et al. (2015). It features a realistic geometry of the subducting slab (Hayes et al., 2012), topography, bathymetry, and the continental Moho

boundary (Tassara & Echaurren, 2012). One-sided and sparse data, simplified Green's functions, and the necessity to regularize the inversion provide at best a low-pass filtered version of the real inter-seismic slip deficit accumulation behavior. A checkerboard synthetic slip model indicates that anomalies of about 50 km in size can be resolved immediately sea- and land-ward along the coast but are unresolved and smeared towards the trench (Figure S6). The highest locking degree (≥0.98) correlates with the highest slip zone, which was seismically quiet prior to the mainshock (Figure 1f, S7).

2.3 Modeling stresses on the megathrust and continental crust due to subduction of an asperity

To relate coupling of an asperity to seismicity, we modeled stresses due to the progressive inter-seismic loading based on both 2D and 3D FE mechanical models. The steady inter-seismic subduction of the oceanic plate is simulated by applying the Elastic Subducting Plate Model of (Kanda & Simons, 2010) with a convergence velocity of 66 mm/a (Figure S5). To simulate the stick-slip behavior, we specified a fault interface with a static friction constitutive model along the seismogenic zone (e.g. Moreno et al., 2018). A higher effective coefficient of friction was used to couple a defined asperity (guided by the co-seismic slip model). We applied normal tractions consistent with the overburden (lithostatic load) as initial stress state along the frictional fault. The model produces shear tractions proportional to the fault normal traction plus cohesive stress (Aagaard et al. 2016). For simplicity, our model neglects gravitational body forces and only deals with stress changes as perturbations to the absolute state of background stress.

We tested different values for the constitutive parameters (effective coefficient of friction and cohesive stress) for a 2D model of 200 yr of steady inter-seismic subduction. Our tests indicate that when the effective coefficient of friction is greater than 0.09, the subduction of the slab is insufficient to cause the fault (F1 in Figure S5a) to slip, the asperity is fully locked for the entire simulation, and slip remains essentially zero after the 200 yrs of loading. Lower values for the effective coefficient of friction allow the interface to fail before the simulation time.

In a 2D model the asperity is simulated on the plate interface between depths of 30-40 km (Figure S5a). The resulting surface displacement, plate interface tractions, and plate interface slip following 200 yrs of simulated time are shown in Figure S8. Modelled horizontal and vertical displacements are consistent with the patterns observed in real subduction zones during the inter-seismic period (e.g., Kanda and Simons, 2010). The shear tractions on the plate interface are highest at the asperity, especially at the upper and lower edges, with the peak shear traction being at the downdip edge of the asperity. The model predicts increased shear tractions by several MPa in the hanging wall roughly where the first and largest foreshock nucleated (Figure S9).

We apply the general set-ups of the 2D model to our 3D case study using the same model geometry (Figure S5b, c) as in the locking inversion. The sense of motion on the simulated megathrust is consistent with the azimuth and rate of plate convergence. We defined the asperity boundaries as the 3.5 m slip contour of the 2014 earthquake (Duputel et al., 2015; Figure 2). Results show that after 200 yrs of loading, positive Coulomb failure stress (CFS) is accumulated along the rim of the asperity with a maximum of ~17 MPa at the downdip margin. This region correlates well with the up-dip limit of the inter-seismic earthquake activity. The foreshocks skirt the upper rim that also shows increased CFS (Figure 2). The region up-dip of the asperity is shielded and slips at a much lower rate producing a partially kinematically locked zone that

extends significantly further updip than the fully coupled asperity (blue contours in Figure 2). This zone was seismically quiet until the foreshock sequence started.

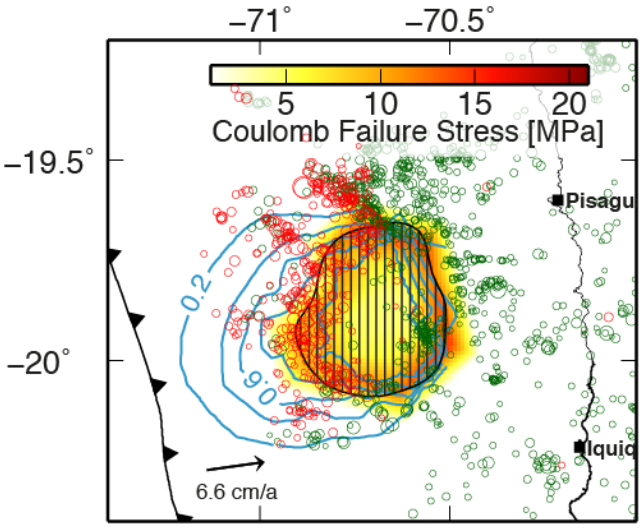

Figure 2. Map with mechanical modeling results. The hashed region is the simulated asperity (3.5 m slip contour, Duputel et al. (2015)) that is coupled while the lower plate subducted at plate velocity. Color map is the resulting Coulomb failure stress on the plate interface after 200 years loading. Light blue contours are the resulting locking degree. Earthquakes as in Figure 1c).

2.3 Correlation of slip with crustal structure

Seismic activity leading up to and during the 2014 earthquake is co-located with the residual gravity anomaly, with the co-seismic slip high correlated with an ~40 mgal gravity low encircled by a relative gravity high that is correlated with the Mogi doughnut seismicity (Figure 1f). The residual gravity anomaly was calculated by removing the effect of the ocean from the free-air gravity anomaly and the residual gravity calculated by replacing both the ocean and the subducted slab with rock having a density of 2700 kg/m^3, thus highlighting density variations due to variations in crustal structure within the forearc wedge (Figure S10). Seismic reflection data (Tréhu et al., 2017); Figures S11-S12) show that the gravity low is approximately coincident with a local sub-basin within the much larger Arica/Iquique Basin (Moberly et al., 1982). That this local sub-basin is still actively subsiding is suggested by approximately horizontal sedimentation in a local topographic depression, which contrasts with tilted and deformed strata and seafloor erosion observed adjacent to the sub-basin.

3 Discussion

We interpret the patch of high co-seismic slip, which was locked and seismically quiet in the years prior to the earthquake, as the main asperity responsible for the 2014 Iquique earthquake. The correlation between observed (seismicity, gravity) and derived (slip, locking, CFS) parameters provides stronger constraints on the location and size of the asperity than can be obtained from any individual data set. Guided by our modeling results, we explain the spatio-temporal distribution of seismicity and modes of slip in the Iquique earthquake region with a simple conceptual model. We note that a similar model was suggested by Dmowska and Li (1982) almost four decades ago, when observational capabilities did not allow verification to the

level of detail possible today. Consider a subducting slab that is coupled to the upper plate across an elliptical patch, but is allowed to creep elsewhere (Figure 3). As it subducts, strain builds up around the asperity with a maximum along its down-dip margin (Figure 3). Slab pull is generally assumed to drive subduction and has been invoked to explain the Iquique earthquake sequence (Bouchon et al., 2016). In the strained regions we expect earthquakes. This is what we observe in the years preceding the Iquique event, where earthquakes and repeaters occur on the plate interface in front of the asperity relatively continuously. Strain is also expected along the asperity's flanks (north and south), where earthquakes do occur, although more clustered in space and time (Figure 1a, g). Socquet et al. (2017) found accelerated aseismic slip starting eight months before the mainshock and located on either side of the asperity (Figure 1d) in accordance with the seismicity clusters. Approximately the same regions showed also the bulk of post-seismic slip (Hoffmann et al., 2018; Shrivastava et al., 2019) (Figure 1d), indicating that the subduction fault moves here at least in part aseismically and that a phase of creep around the asperity driven by slab pull may have begun in the months before the mainshock, further stressing its margins.

What is the significance of the first upper plate foreshock in relation to the following pre-seismic inter-plate sequence that closed the "Mogi doughnut" around the updip half of the asperity? This region of the plate interface was seismically quiet until two weeks before the mainshock. Here the coupled patch is expected to cast a stress shadow (Figure 3) (Bürgmann et al., 2005; Hetland & Simons, 2010; Wang & Tréhu, 2016) generally inhibiting seismicity. Accumulated elastic strain eventually gets relaxed by breaking the weakest part of the system, which generally constitutes the megathrust fault in subduction zones. However, if the asperity is particularly strong, strain may, at least partly, be relaxed by breaking the upper plate. The first large foreshock occurred updip and above the asperity where modeling predicts significantly increased shear tractions on planes comparable to the foreshock mechanism (Figure S9). Forearc wedges are known to contain splay faults, and one of these may have ruptured before the megathrust. Our modeling shows that inter-seismic CFS on the megathrust was increased along the asperity's upper edge (Figure 2,S8e). An additional slight increase induced by the upper plate foreshock (González et al., 2015; Herman et al., 2015) might have triggered the pre-seismic sequence along the pre-stressed upper rim. The degree of stressing of the upper rim depends on the frictional contrast across it and the force balance between ridge push and slab pull, which is about equal in our kinematic plate model representation. Dominance of slab pull would cause lower stresses updip compared to downdip of the asperity, explaining the extended seismic quiescence. Updip, normal stress is also decreased (Figure S8f), lowering friction and possibly promoting stable slip in a conditionally stable environment (Scholz, 1998). Repeating events (Kato et al., 2016; Kato & Nakagawa, 2014; Meng et al., 2015; Figure 1) as well as observed GPS surface displacement transients (Bedford et al., 2015; Herman et al., 2015; S. Ruiz et al., 2014) during the foreshock sequence suggest that aseismic slip was accompanying or even driving the pre-seismic activity. Dynamic seismic cycle simulations using rate-and-state friction laws showed that frictionally locked asperities get eroded at the margins by creep penetrating at the late stage of the seismic cycle (Hori & Miyazaki, 2010; Lapusta & Liu, 2009; Mavrommatis et al., 2017). Our observed inter- and pre-seismic activity is likely an expression of this erosion process.

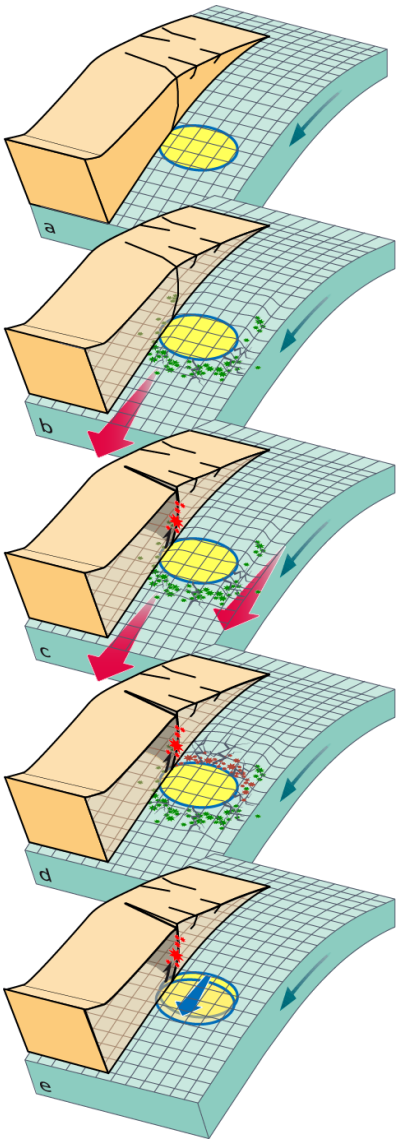

Figure 3. Conceptual model explaining observations of spatio-temporal behavior of pre-event seismicity. **a)** Upper and lower plate are locked across an elliptical asperity (yellow) and allowed to creep everywhere else. **b)** As lower plate subducts, strain is built up down-dip and to the sides of the asperity, whereas the region up-dip of the asperity is shielded. Seismicity occurs in the stressed regions. **c)** If plates are locked strongly across asperity, the upper plate may break first in order to relax the system. **d)** Seismicity infringes onto the plate interface up-dip of the asperity and closes the "Mogi-doughnut". **e)** Asperity breaks in mainshock.

The completion of the Mogi Doughnut around the Iquique earthquake might be a special case. Here, stresses in the upper plate that likely resulted from crustal heterogeneity were released and projected by foreshocks onto a portion of the megathrust that would otherwise be in a stress shadow. This triggered further foreshocks now on the megathrust that closed the 'doughnut.' The down-dip half, however, maybe symptomatic for critically stressed asperities. We consider it worthwhile to search for such crescent-shaped patterns of seismicity as illustrated

in Figure 1a) along well monitored seismic gaps to identify asperities in conjunction with geodetic measurements.

The correlation between the residual gravity anomalies and the Iquique earthquake sequence indicates geological control on inter-plate coupling. Seismic reflection data suggest the presence of subducted seamounts in the region of the Iquique earthquake sequence (Geersen et al., 2015). A rough subducting plate has been associated with fracturing of the upper plate and a weak plate boundary (see review by Wang and Bilek (2014)). Because of the relatively high density of oceanic crust compared to most forearc wedge materials, subducted seamounts should produce forearc gravity highs. The high gravity ring that corresponds to the "Mogi doughnut" identified in this paper may result, at least in part, from topography on the subducted plate in addition to the shallow sedimentary basin imaged in the seismic reflection data (Figure S11). Initiation of the mainshock at the edge of a gravity low and the close correspondence between the patch of greatest slip and the low is consistent with a global pattern first recognized by Wells et al. (2003) and Song and Simons (2003) and interpreted to indicate geological control on the location of asperities. Wells et al. (2003) interpreted the correlation between slip and gravity lows to indicate basal erosion of the upper plate in response to locally high friction on these patches of the megathrust, an association that is supported by our observations. The fundamental geologic reason for these associations, however, remains enigmatic.

4 Conclusions

Seismicity preceding the 2014 M8.1 Iquique earthquake formed a distinct ring around a quiet zone, a pattern known as a Mogi doughnut. The down-dip half of the doughnut was activated during the seven-year observation period leading up the event, whereas its up-dip half was formed during a two-week long foreshock sequence initiated by a M6.7 upper plate event. The doughnut's hole broke with up to 12 m of slip in the mainshock. There is a striking correlation between the pre-mainshock quiet region, the patch of strongest inter-seismic locking, the co-seismic high-slip patch, and a pronounced forearc gravity low. Together these observations provide a rare opportunity to locate a major subduction zone asperity with high confidence. The gravity data imply that this asperity is persistent and related to crustal structure, although the details of this structure cannot be constrained by gravity data alone. Mechanical modeling of asperity loading shows that CFS accumulates around the asperity where we observed inter- and pre-seismic activity. Most features of the spatiotemporal seismicity pattern can be well explained by stress accumulation on the asperity as subduction is driven by slab pull. These observations may provide clues to the future behavior of other well monitored subduction zone segments.

Acknowledgments and Data

We thank the IPOC initiative collecting the high quality seismic and geodetic data and Z. Duputel for providing his slip model. AMT thanks the U.S. National Science Foundation for support through grants OCE-1130013 and OCE-1459368, the participants of cruise MGL1610 for assistance in acquiring and processing the seismic reflection data, and Alexander de Moor for his assistance in developing the software to process the gravity data. MM acknowledges support from FONDECYT 1181479 and ANILLO ACT192169 projects. The catalog of relocated seismicity generated and analyzed in this study as well as the inter-seismic locking map can be accessed from Schurr et al. (XXX). Seismic waveform data were taken from networks CX (GFZ

German Research Centre for Geosciences & Institut des Sciences de l'Univers-Centre National de la Recherche CNRS-INSU, 2006), IQ (Cesca et al., 2009), and GE (GEOFON Data Centre, 1993) accessed via EIDA webservices (e.g., https://geofon.gfz-potsdam.de/), as well as from Chilean Seismological Network (C, C1) stations (Barrientos, 2018) accessed via IRIS webservices (http://ds.iris.edu/SeismiQuery/).

References

Aagaard, B. T., Knepley, M. G., & Williams, C. A. (2013). A domain decomposition approach to implementing fault slip in finite-element models of quasi-static and dynamic crustal deformation. *Journal of Geophysical Research: Solid Earth*, *118*(6), 3059–3079. https://doi.org/10.1002/jgrb.50217

Aagaard, B., S. Kientz, M. Knepley, S. Somala, L. Strand, and C. Williams (2016), Pylith user manual, version 1.9.0. Computational Infrastructure for Geodynamics (CIG), Univ. of California, Davis. [Available at http://www.geodynamics.org/cig/software/pylith/ pylith-manual.pdf.]

Barrientos, S. (2018). The Seismic Network of Chile. *Seismological Research Letters*, *89*(2A), 467–474. https://doi.org/10.1785/0220160195

Bedford, J., Moreno, M., Schurr, B., Bartsch, M., & Oncken, O. (2015). Investigating the final seismic swarm before the Iquique-Pisagua 2014 Mw 8.1 by comparison of continuous GPS and seismic foreshock data. *Geophysical Research Letters*, *42*(10), 3820–3828. https://doi.org/10.1002/2015GL063953

Blakely, R.J. (1996), Potential theory in gravity and magntic applications. Cambridge University Press.

Bouchon, M., Marsan, D., Durand, V., Campillo, M., Perfettini, H., Madariaga, R., & Gardonio, B. (2016). Potential slab deformation and plunge prior to the Tohoku, Iquique and Maule earthquakes. *Nature Geoscience*, *9*(5), 380–383. https://doi.org/10.1038/ngeo2701

Bürgmann, R., Kogan, M. G., Steblov, G. M., Hilley, G., Levin, V. E., & Apel, E. (2005). Interseismic coupling and asperity distribution along the Kamchatka subduction zone. *Journal of Geophysical Research: Solid Earth*, *110*(7), 1–17. https://doi.org/10.1029/2005JB003648

Cesca, S., Sobiesiak, M., Tassara, A., Olcay, M., Günther, E., Mikulla, S., Dahm, T., (2009). The Iquique Local Network and PicArray. GFZ Data Services. Other/Seismic Network. https://doi.org/10.14470/VD070092

Contreras-Reyes, E., Jara, J., Grevemeyer, I., Ruiz, S., & Carrizo, D. (2012). Abrupt change in the dip of the subducting plate beneath north Chile. *Nature Geoscience*, *5*(5), 342–345. https://doi.org/10.1038/ngeo1447

De Moor, A., (2015). Local seismicity recorded by ChilePEPPER: Implications for dynamic accretionary prism response and long-term prism evolution, MS thesis, Oregon State University, 79 pp. [https://ir.library.oregonstate.edu/xmlui/handle/1957/58092].

Dmowska, R., & Li, V. C. (1982). A mechanical model of precursory source processes for some large earthquakes. Geophysical Research Letters, 9(4), 393–396. https://doi.org/10.1029/GL009i004p00393

Dmowska, R., & Lovison, L. C. (1992). Influence of asperities along subduction interfaces on the stressing and seismicity of adjacent areas. *Tectonophysics*, *211*(1–4), 23–43. https://doi.org/10.1016/0040-1951(92)90049-C

Duputel, Z., Jiang, J., Jolivet, R., Simons, M., Rivera, L., Ampuero, J. P., et al. (2015). The

Iquique earthquake sequence of April 2014: Bayesian modeling accounting for prediction uncertainty. *Geophysical Research Letters*, *42*(19), 7949–7957. https://doi.org/10.1002/2015GL065402

Geersen, J., Ranero, C. R., Barckhausen, U., & Reichert, C. (2015). Subducting seamounts control interplate coupling and seismic rupture in the 2014 Iquique earthquake area. *Nature Communications*, *6*, 2–7. https://doi.org/10.1038/ncomms9267

GEOFON Data Centre (1993). GEOFON seismic network. Deutsches GeoForschungsZentrum GFZ. Other/Seismic Network. https://doi.org/10.14470/TR560404.

GFZ German Research Centre For Geosciences, Institut Des Sciences De L'Univers-Centre National De La Recherche CNRS-INSU (2006). IPOC seismic network, https://doi.org/10.14470/pk615318.

González, G., Salazar, P., Loveless, J. P., Allmendinger, R. W., Aron, F., & Shrivastava, M. N. (2015). Upper plate reverse fault reactivation and the unclamping of the megathrust during the 2014 northern Chile earthquake sequence. *Geology*, *43*(8), 671–674. https://doi.org/10.1130/G36703.1

González, E. (1989). Hydrocarbon resources in the coastal zone of Chile. In G. E. Ericksen, M. T. Canas Pinochet, & J. A. Reinemund (Eds.), Geology of the Andes and its relation to hydrocarbon and mineral resources (p. 383). Houston, Texas: Circum Pacific Council Publications.

Hayes, G. P., Wald, D. J., & Johnson, R. L. (2012). Slab1.0: A three-dimensional model of global subduction zone geometries. *Journal of Geophysical Research: Solid Earth*, *117*(B1), n/a-n/a. https://doi.org/10.1029/2011JB008524

Hayes, G. P., Herman, M. W., Barnhart, W. D., Furlong, K. P., Riquelme, S., Benz, H. M., et al. (2014). Continuing megathrust earthquake potential in Chile after the 2014 Iquique earthquake. *Nature*, *512*(7514), 295–298. https://doi.org/10.1038/nature13677

Herman, M. W., Furlong, K. P., Hayes, G. P., & Benz, H. M. (2015). Foreshock triggering of the 1 April 2014 Mw 8.2 Iquique, Chile, earthquake. *Earth and Planetary Science Letters*, *447*(April 2014), 119–129. https://doi.org/10.1016/j.epsl.2016.04.020

Hetland, E. A., & Simons, M. (2010). Post-seismic and interseismic fault creep II: Transient creep and interseismic stress shadows on megathrusts. *Geophysical Journal International*, *181*(1), 99–112. https://doi.org/10.1111/j.1365-246X.2009.04482.x

Hoffmann, F., Metzger, S., Moreno, M., Deng, Z., Sippl, C., Ortega-Culaciati, F., & Oncken, O. (2018). Characterizing Afterslip and Ground Displacement Rate Increase Following the 2014 Iquique-Pisagua Mw8.1 Earthquake, Northern Chile. *Journal of Geophysical Research: Solid Earth*, *123*(5), 4171–4192. https://doi.org/10.1002/2017JB014970

Hori, T., & Miyazaki, S. (2010). Hierarchical asperity model for multiscale characteristic earthquakes: A numerical study for the off-Kamaishi earthquake sequence in the NE Japan subduction zone. *Geophysical Research Letters*, *37*(10), 2–7. https://doi.org/10.1029/2010GL042669

Husen, S., Kissling, E., Flueh, E. R., & Asch, G. (1999). Accurate hypocentre determination in the seismogenic zone of the subducting Nazca Plate in northern Chile using a combined on-/offshore network. *Geophysical Journal International*, *138*(3), 687–701. https://doi.org/10.1046/j.1365-246x.1999.00893.x

Jara, J., Sánchez-Reyes, H., Socquet, A., Cotton, F., Virieux, J., Maksymowicz, A., et al. (2018). Kinematic study of Iquique 2014 Mw 8.1 earthquake: Understanding the segmentation of the seismogenic zone. *Earth and Planetary Science Letters*, *503*, 131–143.

https://doi.org/10.1016/j.epsl.2018.09.025
Kanamori, H. (2013). The Nature of Seismicity Patterns Before Large Earthquakes. In *Earthquake prediction: an international review* (Vol. 4, pp. 1–19). https://doi.org/10.1029/ME004p0001
Kanda, R. V. S., & Simons, M. (2010). An elastic plate model for interseismic deformation in subduction zones. *Journal of Geophysical Research: Solid Earth*, *115*(3), 1–19. https://doi.org/10.1029/2009JB006611
Kato, A., & Nakagawa, S. (2014). Multiple slow-slip events during a foreshock sequence of the 2014 Iquique, Chile M w 8.1 earthquake. *Geophysical Research Letters*, *41*(15), 5420–5427. https://doi.org/10.1002/2014GL061138
Kato, A., Fukuda, J., Kumazawa, T., & Nakagawa, S. (2016). Accelerated nucleation of the 2014 Iquique, Chile Mw 8.2 Earthquake. *Scientific Reports*, *6*(April), 1–9. https://doi.org/10.1038/srep24792
Kendrick, E., Bevis, M., Smalley, R., & Brooks, B. (2001). An integrated crustal velocity field for the central Andes. *Geochemistry, Geophysics, Geosystems*, *2*(11). https://doi.org/10.1029/2001GC000191
Lapusta, N., & Liu, Y. (2009). Three-dimensional boundary integral modeling of spontaneous earthquake sequences and aseismic slip. *Journal of Geophysical Research: Solid Earth*, *114*(9), 1–25. https://doi.org/10.1029/2008JB005934
Lay, T., & Kanamori, H. (1981). An asperity model of large earthquake sequences. *Earthquake Prediction: An International Review*, *4*, 579–592.
Lay, T., Yue, H., Brodsky, E. E., & An, C. (2014). The 1 April 2014 Iquique, Chile, Mw 8.1 earthquake rupture sequence. *Geophysical Research Letters*, *7*(April), 1–8. https://doi.org/10.1002/2014GL060238
Li, S., Moreno, M., Bedford, J., Rosenau, M., & Oncken, O. (2015). Revisiting viscoelastic effects on interseismic deformation and locking degree: A case study of the peru-north chile subduction zone. *Journal of Geophysical Research: Solid Earth*, *120*(6), 4522–4538. https://doi.org/10.1002/2015JB011903
Mavrommatis, A. P., Segall, P., & Johnson, K. M. (2017). A Physical Model for Interseismic Erosion of Locked Fault Asperities. *Journal of Geophysical Research: Solid Earth*, *122*(10), 8326–8346. https://doi.org/10.1002/2017JB014533
Meng, L., Huang, H., Bürgmann, R., Ampuero, J. P., & Strader, A. (2015). Dual megathrust slip behaviors of the 2014 Iquique earthquake sequence. *Earth and Planetary Science Letters*, *411*, 177–187. https://doi.org/10.1016/j.epsl.2014.11.041
Métois, M., Socquet, A., Vigny, C., Carrizo, D., Peyrat, S., Delorme, A., et al. (2013). Revisiting the North Chile seismic gap segmentation using GPS-derived interseismic coupling. *Geophysical Journal International*, *194*(3), 1283–1294. https://doi.org/10.1093/gji/ggt183
Moberly, R., Shepherd, G.L., & Coulbourn, W.T. (1982). Forearc and other basins, continental margin of northern and southern Peru and adjacent Ecuador and Chile. Geological Society, London, Special Publications (10), 171-189. https://doi.org/10.1144/GSL.SP1982.010.01.11
Mogi, K. (1969). Some features of recent seismic activity in and near Japan (2) Activity before and after Great Earthquakes. *Bull. Earthq. Res. Inst.*, *47*(4), 395–417.
Moreno, M., Li, S., Melnick, D., Bedford, J. R., Baez, J. C., Motagh, M., et al. (2018). Chilean megathrust earthquake recurrence linked to frictional contrast at depth. *Nature Geoscience*, *11*(4), 285–290. https://doi.org/10.1038/s41561-018-0089-5
Nábělek, J. L., & Xia, G. (1995). Moment-tensor analysis using regional data: Application to the

25 March, 1993, Scotts Mills, Oregon, earthquake. *Geophysical Research Letters*, *22*(1), 13–16.
Ruiz, J., Maksymowicz, A., Ortega-Culaciati, F., Rivera, L., & Comte, D. (2019). Source characteristics of the March 16, 2014 Mw 6.7 earthquake and its implications for the Mw 8.2 Pisagua mainshock. *Tectonophysics*, *767*, 228170. https://doi.org/https://doi.org/10.1016/j.tecto.2019.228170
Ruiz, S., & Madariaga, R. (2018). Historical and recent large megathrust earthquakes in Chile. *Tectonophysics*, *733*, 37–56. https://doi.org/10.1016/j.tecto.2018.01.015
Ruiz, S., Métois, M., Fuenzalida, A., Ruiz, J., Leyton, F., Grandin, R., et al. (2014). Intense foreshocks and a slow slip event preceded the 2014 Iquique Mw8.1 earthquake. *Science*, *1165*(6201), 1165–1169. https://doi.org/10.1126/science.1256074
Scholz, C. H. (1998). Earthquakes and friction laws. *Nature*, *391*(6662), 37–42. https://doi.org/10.1038/34097
Schurr, B., Asch, G., Rosenau, M., Wang, R., Oncken, O., Barrientos, S. E., et al. (2012). The 2007 M7.7 Tocopilla northern Chile earthquake sequence: Implications for along-strike and downdip rupture segmentation and megathrust frictional behavior. *Journal of Geophysical Research: Solid Earth*, *117*(B5), 1–19. https://doi.org/10.1029/2011JB009030
Schurr, B., Asch, G., Hainzl, S., Bedford, J., Hoechner, A., Palo, M., et al. (2014). Gradual unlocking of plate boundary controlled initiation of the 2014 Iquique earthquake. *Nature*, *512*(7514), 299–302. https://doi.org/10.1038/nature13681
Shrivastava, M. N., González, G., Moreno, M., Soto, H., Schurr, B., Salazar, P., & Báez, J. C. (2019). Earthquake segmentation in northern Chile correlates with curved plate geometry. *Scientific Reports*, *9*(1), 4403. https://doi.org/10.1038/s41598-019-40282-6
Sippl, C., Schurr, B., Yuan, X., Mechie, J., Schneider, F. M., Gadoev, M., et al. (2013). Geometry of the Pamir-Hindu Kush intermediate-depth earthquake zone from local seismic data. *Journal of Geophysical Research: Solid Earth*, *118*(4), 1438–1457. https://doi.org/10.1002/jgrb.50128
Sippl, C., Schurr, B., Asch, G., & Kummerow, J. (2018). Seismicity Structure of the Northern Chile Forearc From >100,000 Double-Difference Relocated Hypocenters. *Journal of Geophysical Research: Solid Earth*, *123*(5), 4063–4087. https://doi.org/10.1002/2017JB015384
Socquet, A., Valdes, J. P., Jara, J., Cotton, F., Walpersdorf, A., Cotte, N., et al. (2017). An 8 month slow slip event triggers progressive nucleation of the 2014 Chile megathrust. *Geophysical Research Letters*, *44*(9), 4046–4053. https://doi.org/10.1002/2017GL073023
Song, T. R. A., & Simons, M. (2003). Large trench-parallel gravity variations predict seismogenic behavior in subduction zones. *Science*, *301*(5633), 630–633. https://doi.org/10.1126/science.1085557
Soto, H., Sippl, C., Schurr, B., Kummerow, J., Asch, G., Tilmann, F., et al. (2019). Probing the Northern Chile Megathrust With Seismicity: The 2014 M8.1 Iquique Earthquake Sequence. *Journal of Geophysical Research: Solid Earth*, *124*, 2019JB017794. https://doi.org/10.1029/2019JB017794
Tassara, A., & Echaurren, A. (2012). Anatomy of the Andean subduction zone: Three-dimensional density model upgraded and compared against global-scale models. *Geophysical Journal International*, *189*(1), 161–168. https://doi.org/10.1111/j.1365-246X.2012.05397.x
Thatcher, W. (1990). Order and diversity in the modes of Circum-Pacific Earthquake recurrence.

Journal of Geophysical Research, *95*(B3), 2609. https://doi.org/10.1029/JB095iB03p02609
Tréhu, A.M., Vera, E., Riedel, M., & MGL1610 Science Party (2017). MGL1610 Cruise Report, https://www.rvdata.us/search/cruise/MGL1610
Waldhauser, F., & Ellsworth, W. L. (2000). A Double-difference Earthquake location algorithm: Method and application to the Northern Hayward Fault, California. *Bulletin of the Seismological Society of America*, *90*(6), 1353–1368. https://doi.org/10.1785/0120000006
Wang, K., & Bilek, S. L. (2014). Invited review paper: Fault creep caused by subduction of rough seafloor relief. *Tectonophysics*, *610*, 1–24. https://doi.org/10.1016/j.tecto.2013.11.024
Wang, K., & Tréhu, A. M. (2016). Some outstanding issues in the study of great megathrust earthquakes-The Cascadia example. *Journal of Geodynamics*, *98*, 1–18. https://doi.org/10.1016/j.jog.2016.03.010
Wells, R. E., Blakely, R. J., Sugiyama, Y., Scholl, D. W., & Dinterman, P. A. (2003). Basin-centered asperities in great subduction zone earthquakes: A link between slip, subsidence, and subduction erosion? *Journal of Geophysical Research: Solid Earth*, *108*(B10), 1–21. https://doi.org/10.1029/2002JB002072
Yagi, Y., Okuwaki, R., Enescu, B., Hirano, S., Yamagami, Y., Endo, S., & Komoro, T. (2014). Rupture process of the 2014 Iquique Chile Earthquake in relation with the foreshock activity. *Geophysical Research Letters*, *41*(12), 4201–4206. https://doi.org/10.1002/2014GL060274

Supporting Information for

Forming a Mogi Doughnut during the inter- and pre-seismic phase of the 2014 M8.1 Iquique, Northern Chile Earthquake

B. Schurr[1], M. Moreno[2], A. M. Tréhu[3], J. Bedford[1], J. Kummerow[4], S. Li[5], and O. Oncken[1]

[1]Deutsches GeoForschungsZentrum – GFZ, Section Lithosphere Dynamics, Telegrafenberg, 14473 Potsdam, Germany
[2]Universidad de Concepción, Departamento de Geofísica, Concepción, Chile
[3]College of Earth, Ocean, and Atmospheric Sciences, Oregon State University, 104 CEOAS Administration Building, Corvallis, OR 97331-5503
[4]Freie Universität Berlin, Department of Earth Sciences, Berlin, Germany
[5]University of Tokyo, Earthquake Research Institute, Tokyo, Japan

Contents of this file

Figures S1 to S9

Additional Supporting Information (Files uploaded separately)

Dataset S1: netcdf grid file of locking model from Figure S5b.

Introduction

The following figures and data file provide additional information for our main article. In particular, we

- provide images of seismicity with two other slip models,
- a cross section showing only the inter-seismic earthquakes only,
- describe and show results of waveform modeling for the two largest foreshocks additionally constraining the depth difference,
- show the data set and a resolution test for the updated locking model,
- show the detailed set up of the mechanical finite element model in 2D and 3D, and modeling results for the 2D case,
- Comparison between the free-air gravity anomaly and the residual anomaly calculated as described in the text,
- Seismic reflection profiles indicating the presence of a localized sedimentary basin associated with the residual gravity anomaly.

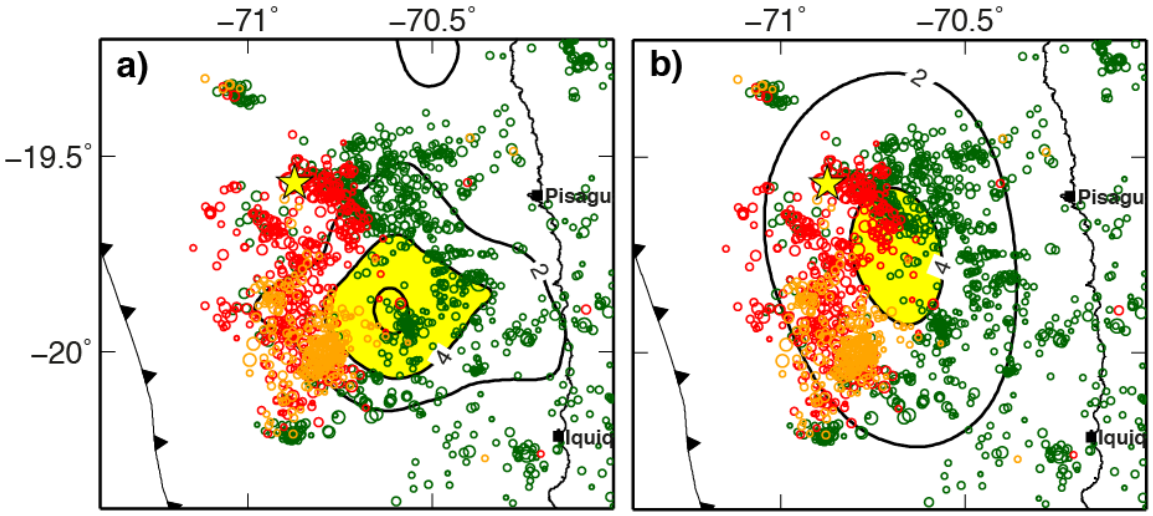

Figure S1. Same as Fig. 1b, but with slip models from a) Liu et al. (2015) and b) Schurr et al. (2014). Regions of slip > 4 m are filled in yellow.

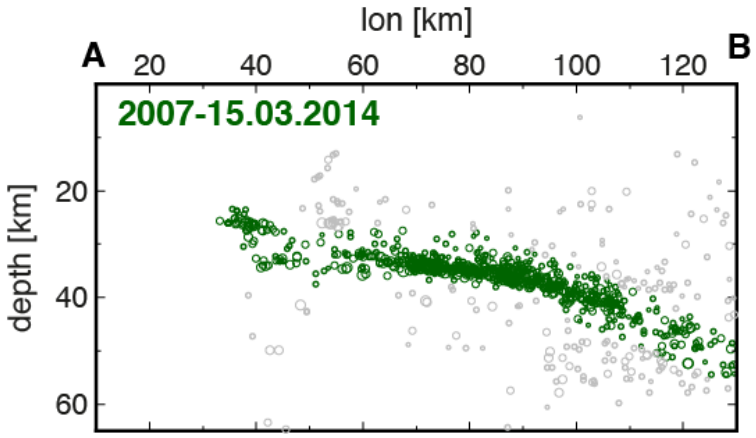

Figure S2. Cross section through inter-seismic seismicity only.

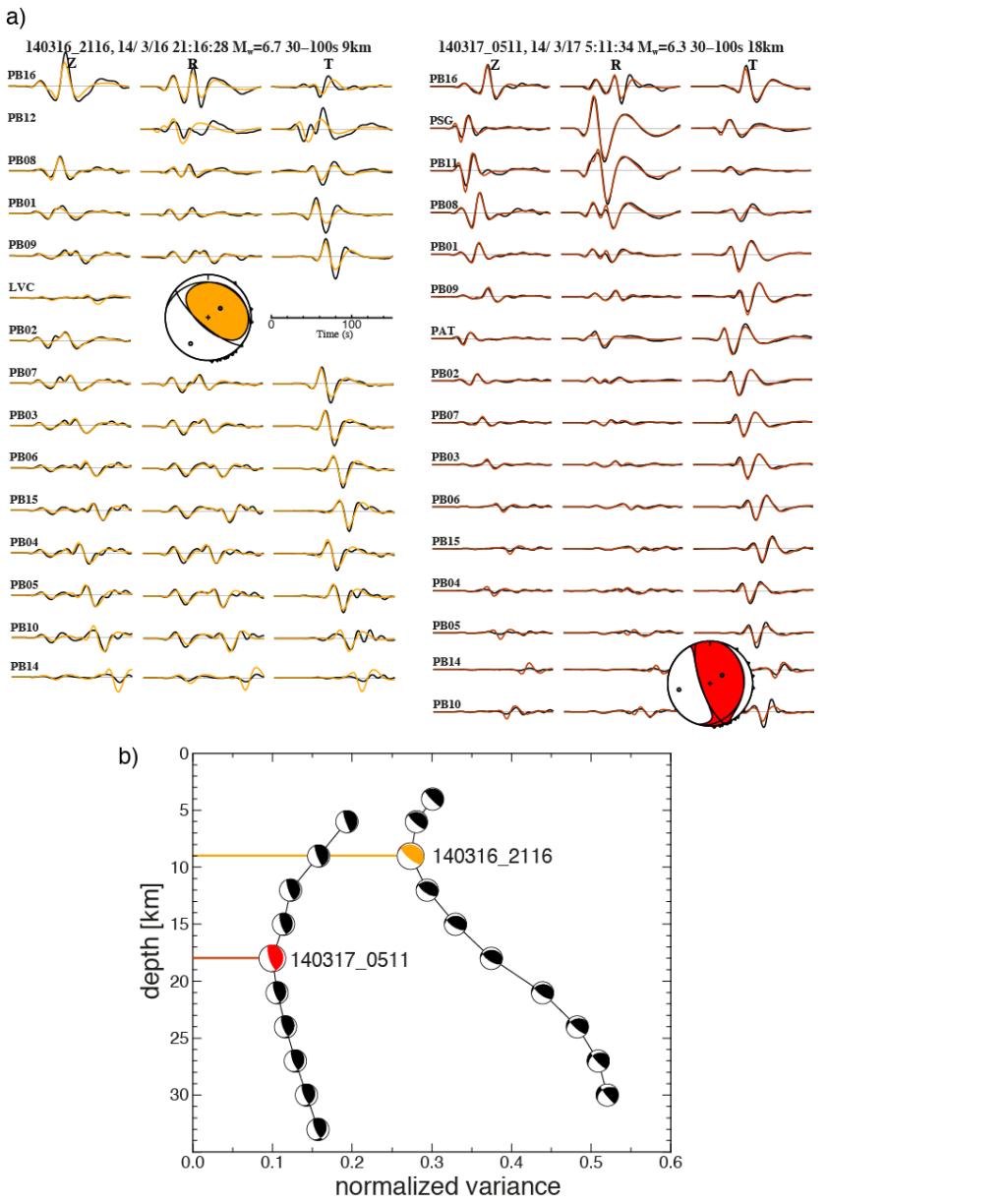

Figure S3. a) Observed (black) and modeled (colored) waveforms for first two large aftershocks. Mechanisms and waveforms differ significantly. b) Normalized variance of fit versus depth. The first foreshock apparently has significantly lower depth than the second, corroborating the inference that it occurred in the upper plate, whereas the second occurred on the plate interface.

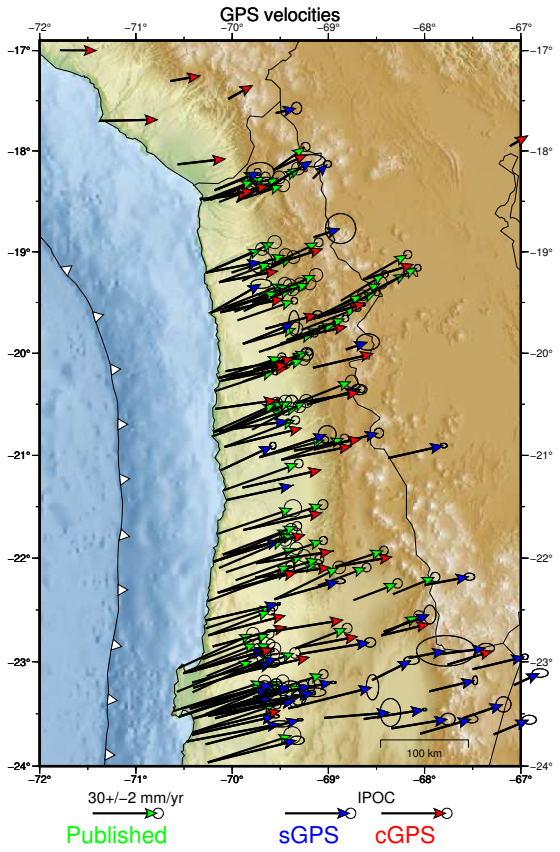

Figure S4. Inter-seismic GPS velocities in a South American reference frame. This velocity field characterizes the deformation in the decade preceding the 2014 Iquique earthquake and consists of the combination of velocities from ~40 continuously recording stations, ~70 survey-type GPS and previous published vectors (Kendrick et al., 2001; Métois et al., 2013).

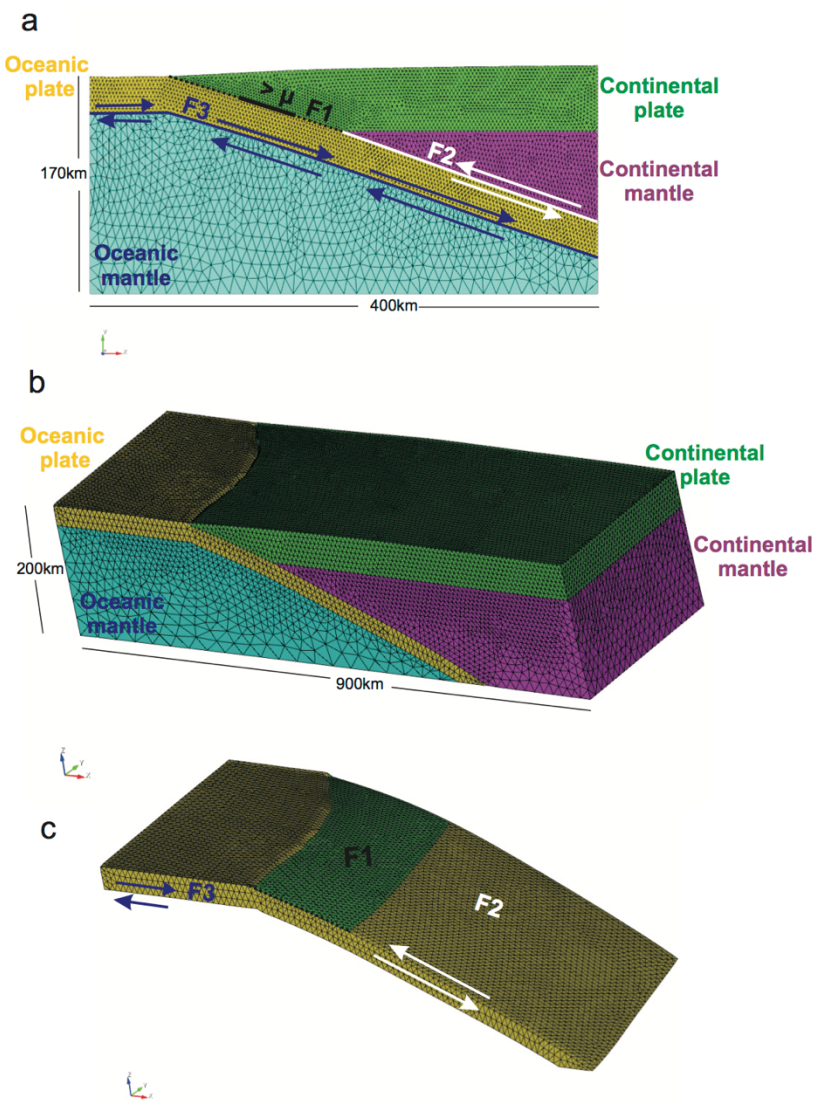

Figure S5. Model set up. a) Schematic plot of the two-dimensional FEM model structure and fault boundary conditions. The model consists of an elastic downgoing slab unit (oceanic plate, 30 km thickness) and an upper crustal unit (overriding continental plate). The downgoing slab and overriding plate sit on top of oceanic and continental asthenospheric units, with a Young's modulus of 120, 100 and 160 GPa, respectively (e.g., Li et al., 2015). We specified two fault interfaces with kinematic fault conditions, representing the base of the slab (F3) and the creeping part of the slab top below the locked zone (F2). On those interfaces, we prescribed a homogeneous constant creeping equal to the plate convergence velocity (6.6 cm/yr). To simulate the stick-slip behaviour of the seismogenic zone, we specified a fault interface (F1) with static friction constitutive model. A coefficient of friction of 0.09 was used for the coupled section and 0.005 for the creeping parts. b-c) Three-dimensional FEM model configuration. Model incorporates geometries of the slab and continental Moho.

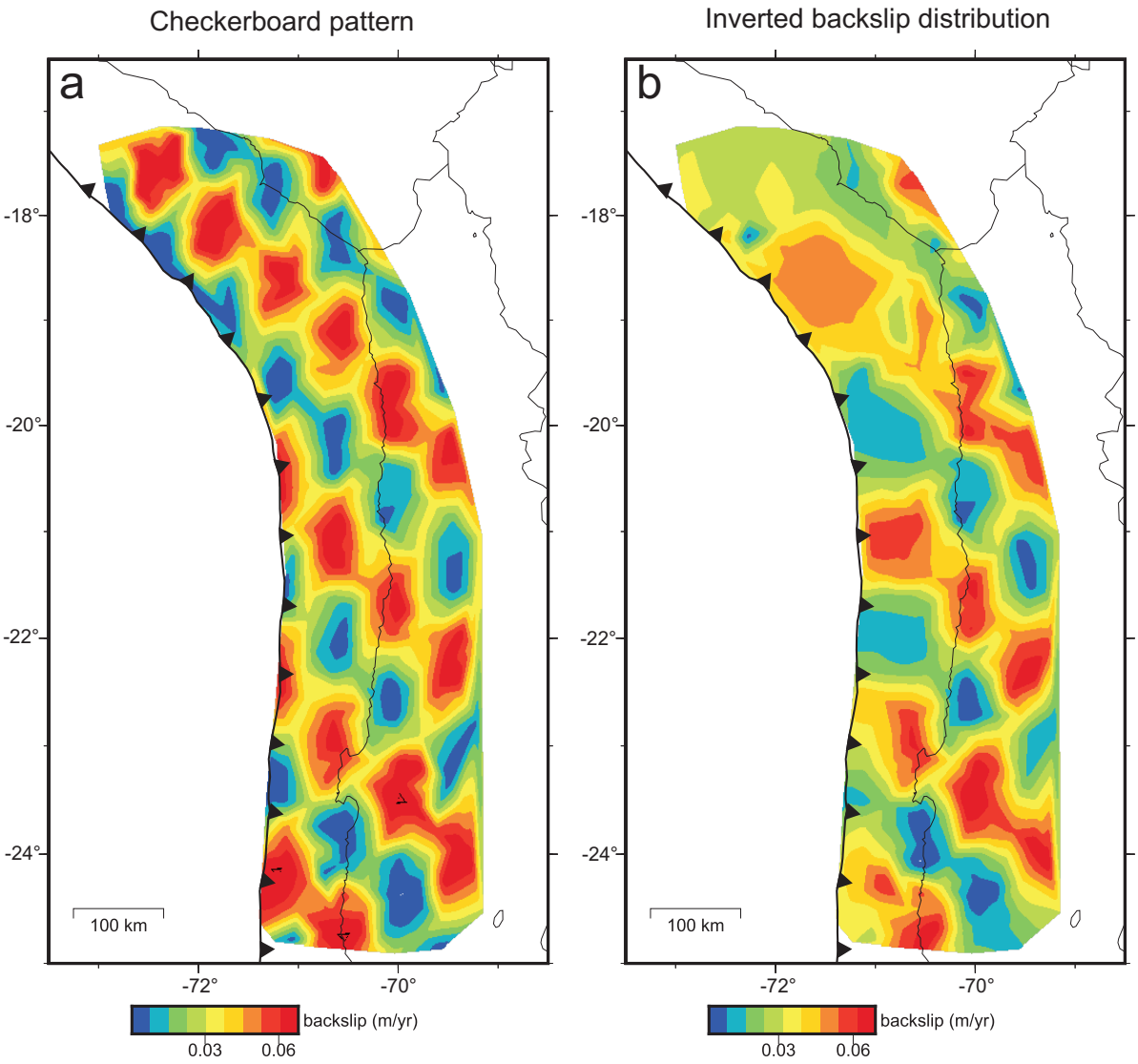

Figure S6. Checkerboard synthetic back slip model to evaluate the model resolution. A) The input locked patches are about 30×30 km in size and assigned with 66 mm/yr back-slip rate. B) Recovered patches from viscoelastic inversion of input locked patches.

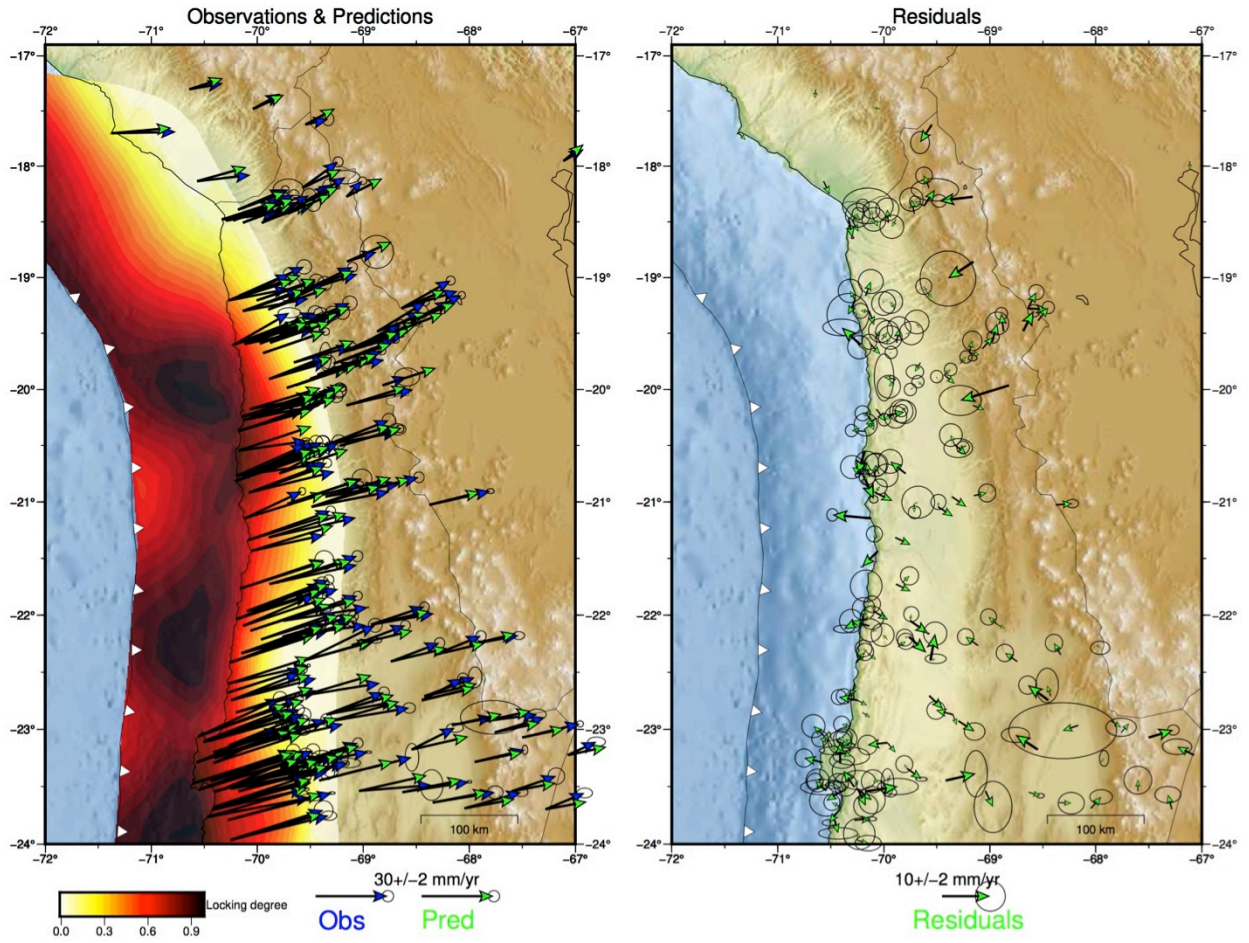

Figure S7. Optimal distribution of locking rate along the plate interface. Predicted interseismic velocities and GPS vectors are shown by green and blue arrows, respectively. Model residuals are shown by green arrows in the right panel.

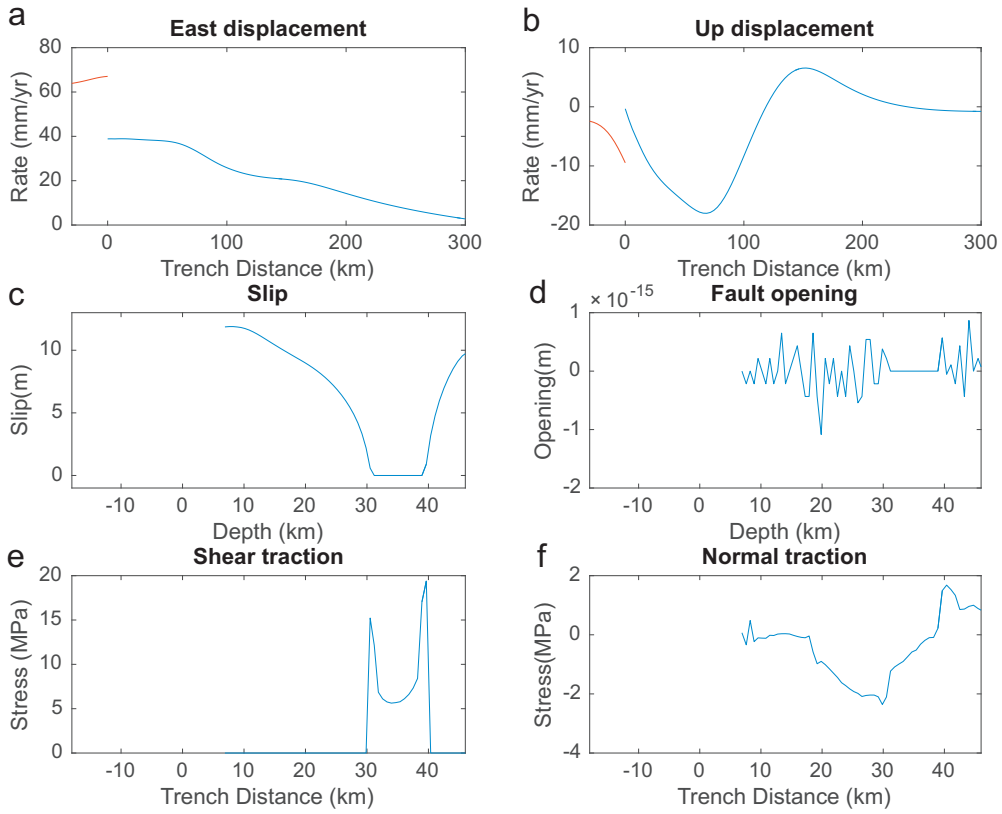

Figure S8. 2D results of 200 yr of subduction of a fully coupled asperity between 30-40 km depth. a-b) Model prediction for horizontal and vertical components of surface displacement. Red and blue lines indicate the displacement in the oceanic and continental plates, respectively. The surface displacements show a gradient of eastward motion, subsidence from the trench with a hinge-line to uplift slightly east of the easternmost extent of the asperity. c-d) Cumulative dip slip and fault opening. Cumulative slip of ~12 m gradually decreases from the trench to zero inside the asperity. The fault remains fully coupled during the entire computation time inside the asperity region. The fault slips only in the down-dip direction, while fault opening is insignificant. e-f) Cumulative shear and normal traction along the frictional fault (F1). Peaks of shear stress occurred in the down-dip and updip of the asperity borders. Lower normal stress is accumulated in the down-dip region (positive normal stresses indicate an unloading).

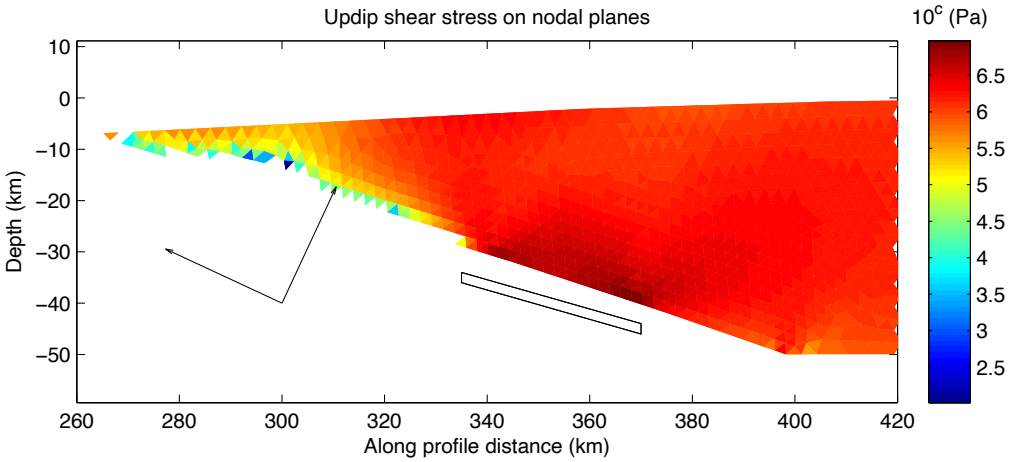

Figure S9. Shear traction (updip positive) on planes inclined 25° and 115° (illustrated by the arrows), comparable to the nodal planes of the March 16th Mw 6.7 event in the upper crust. The shear traction for a defined dip is calculated by multiplying the stress tensor by the unit normal vector of the failure plane and subsequently taking the dot product with the unit vector of the failure plane. Most of the stresses in this region (for the tested angles) are positive and are therefore plotted with logarithmic colour scale (base 10). Positive indicates an increase in shear stress in the updip sense. In the regions updip and in the upper portion of the plate we have shear tractions of one MPa or greater, indicating that a crustal fault here would have accumulated considerable stress in the inter-seismic period.

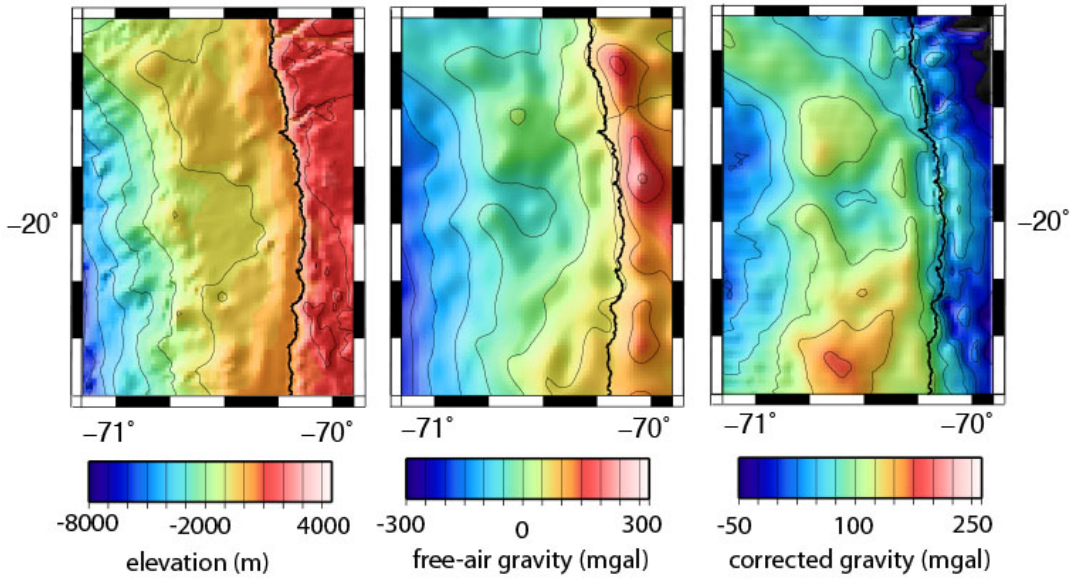

Figure S10. (left) Elevation (GMRT accessed via www.geomapapp.org). (middle) Free-air gravity (Sandwell and Smith v18.1, accessed via www.geomapapp.org). (right) Residual gravity calculated by removing the effect of the ocean by replacing water with rock at a density of 2700 kg/m^3 in rectangular prisms with a cross-sectional area of 1 km^2 that extend from the sea surface to the seafloor (Blakely, 1995). For each grid point, the correction was determined by summing the contribution of adjacent prisms within a radius of 20 km of the data point being corrected, a radius adequate to capture the contribution to the gravitational attraction of the ocean for water depths up to the maximum water depth in the study area (de Moor, 2015). The slab correction was implemented by replacing a density model based on a 2D P-wave velocity model (Contreras-Reyes et al., 2012) for a transect across the forearc near 22°S by a density of 2700 kg/m3 and projecting this correction to the north and south along the axis of the trench.

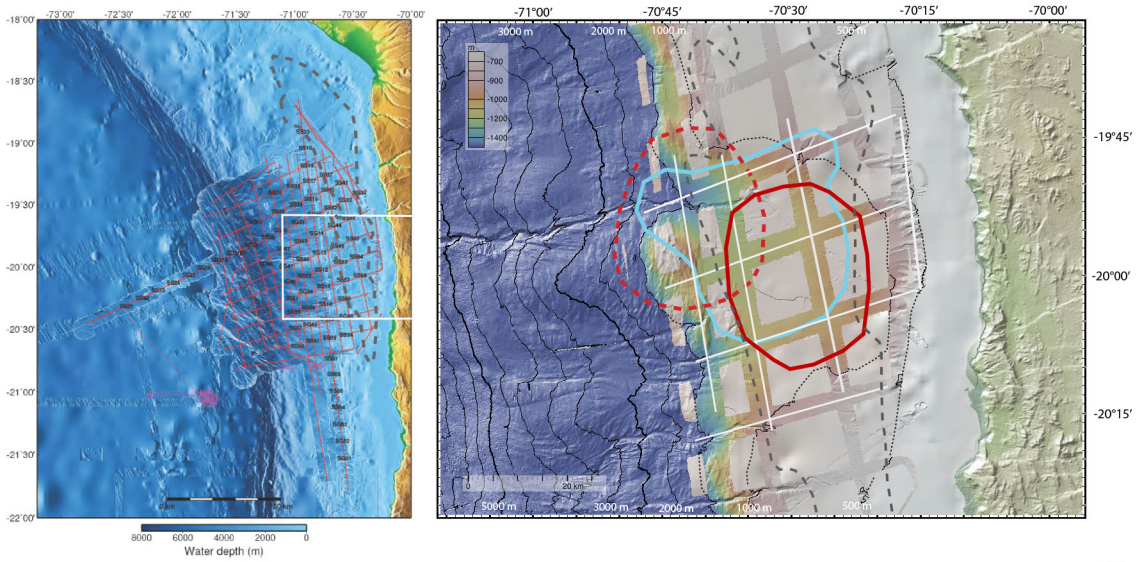

Figure S11. (left) Map showing location of seismic lines acquired during cruise MGL1610 (Tréhu et al., 2017). Numbers indicate positions of ocean bottom seismometers. Thick grey dashed line is the outline of the Arica/Iquique basin of Moberly et al. (1982) [also called the Tarapaca Basin by Gonzalez, 1989]. White box outlines the region shown on the right.
(right) Detailed bathymetric map from swath bathymetry acquired during cruise MGL1610 overlain on the GMRT global elevation model. Note the narrowing of the swath as water depth decreases. Depth contours are shown at 500 m intervals and are dotted where interpolated between the swaths. White lines are the locations of seismic reflection profiles shown in Figure S12. Light blue line is the outline of the gravity low in the center of the 'Mogi Doughnut'. Dashed red line is the 4 m slip contour from Duputel et al. (2015). Solid red line is the approximate outline of a distinct sub-basin located within the region interpreted to be by the much larger Arica/Iquique/Tarapaca basin. Subhorizontal, underformed reflections within a topographic basin suggest continuing basin formation subsidence within this sub-basin.

Figure S12 (following 2 pages) Segments of multichannel profiles from cruise MGL1610 (Tréhu et al., 2017) that cross the 'Mogi Doughnut'. **A.** east-west oriented seismic profiles ordered from north to south. **B.** Segments of north-south oriented seismic profiles ordered from east to west. All profiles represent initial processing of the near 128 channels (source-receiver offsets < 1000m) which have been corrected for normal moveout, stacked, and migrated assuming a velocity of 1500 m/s. Data have been bandpass filtered from 8 to 35 Hz.

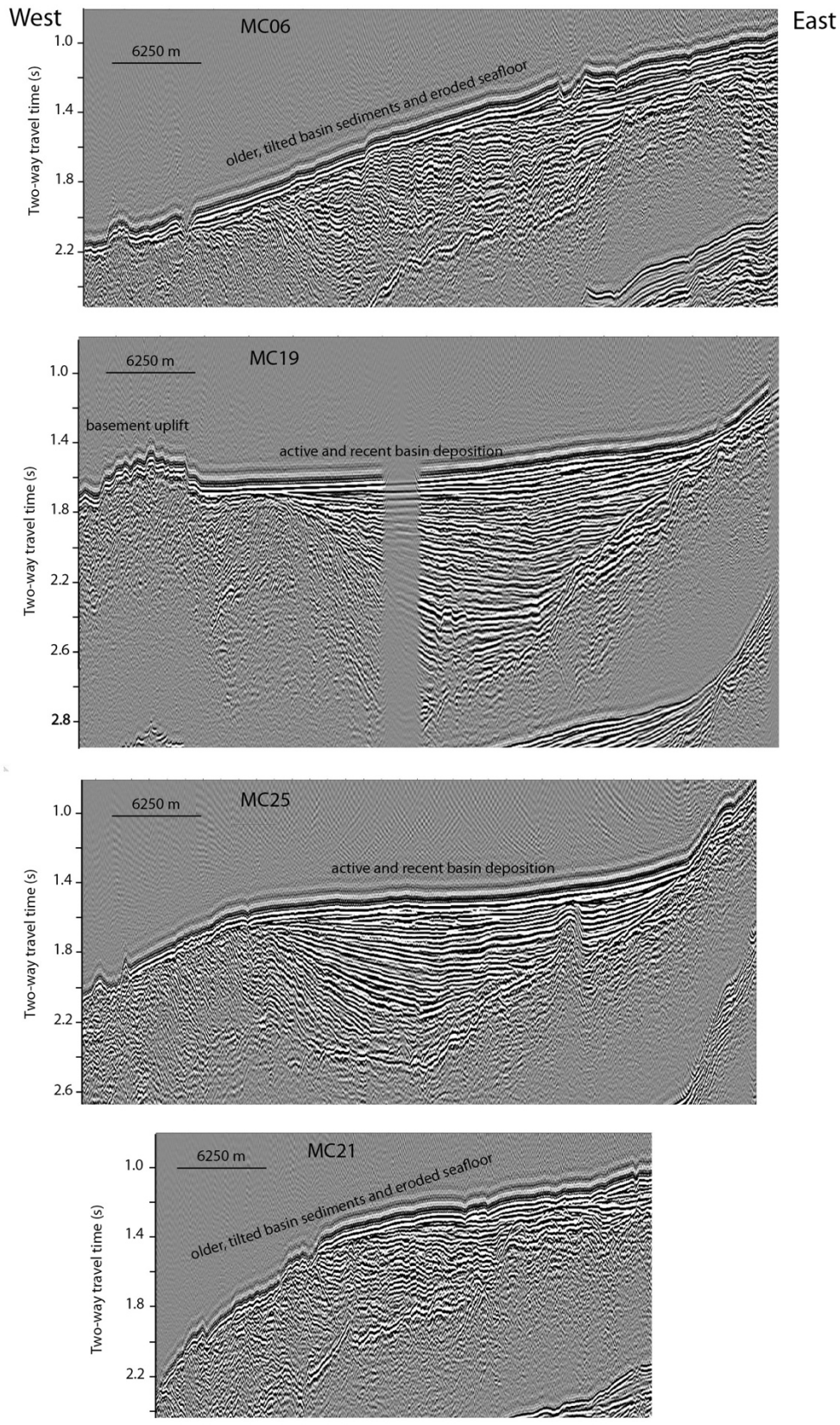
West
East
MC06
6250 m
older, tilted basin sediments and eroded seafloor
Two-way travel time (s)
1.0
1.4
1.8
2.2
MC19
6250 m
basement uplift
active and recent basin deposition
2.6
2.8
MC25
active and recent basin deposition
MC21
older, tilted basin sediments and eroded seafloor

Figure 12A.

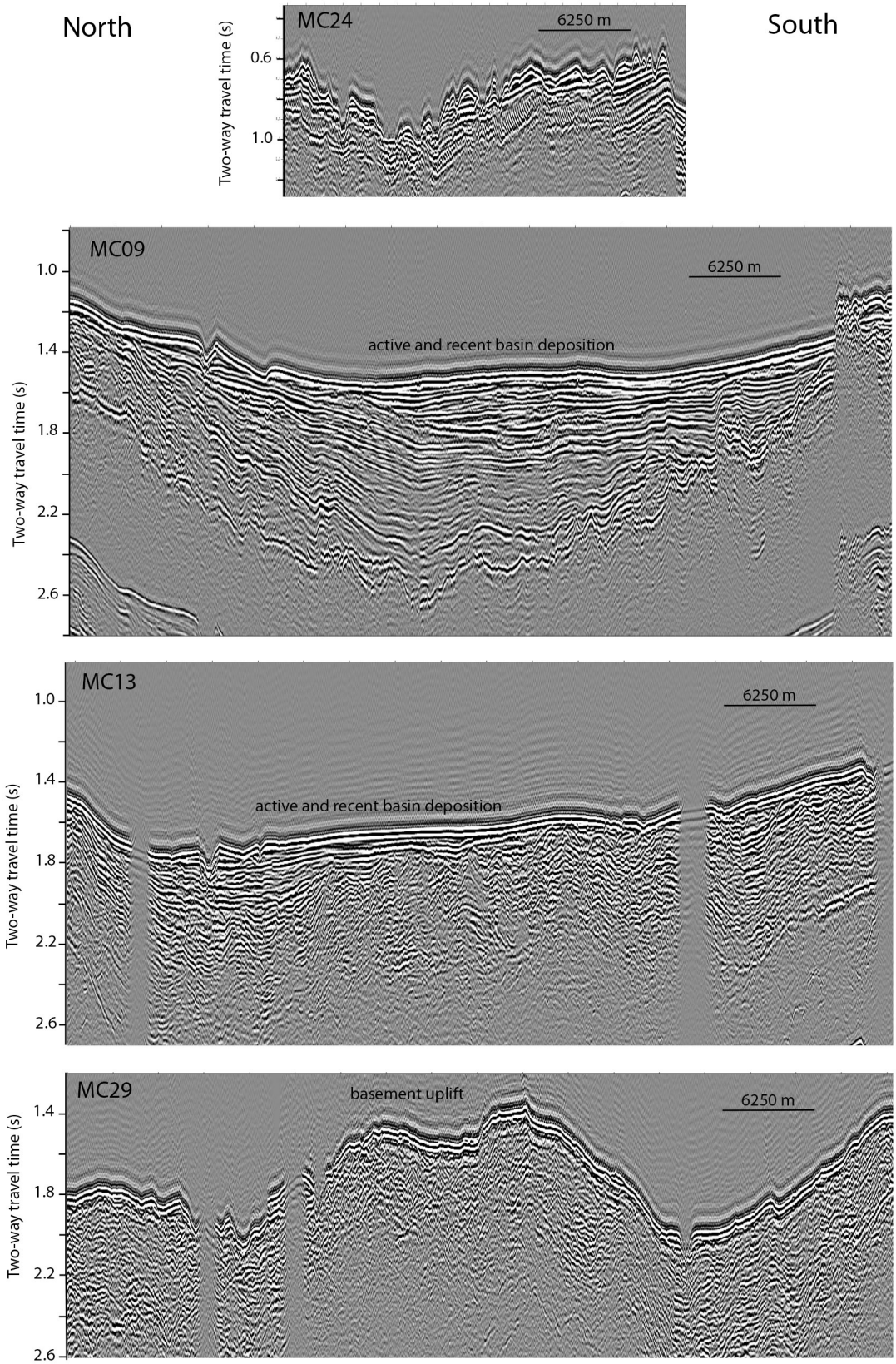
North
South
MC24
6250 m
Two-way travel time (s)
0.6
1.0
MC09
6250 m
active and recent basin deposition
1.0
1.4
1.8
2.2
2.6
MC13
6250 m
active and recent basin deposition
MC29
basement uplift
6250 m

Figure 12B.